Effects of carbon-fibre Z-pins on the through-thickness tensile strength of curved composite laminates under four-point bending

Mudan Chen, Bing Zhang, Giuliano Allegri, Stephen R. Hallett [*]

Bristol Composites Institute, University of Bristol, Queen's Building, Bristol, BS8 1TR, UK

A B S T R A C T

This study investigates the influence of discrete through-thickness reinforcement, i.e. Z-pins, on the through-thickness tensile strength (TTS) of curved laminates through four-point bending experiments. Three types of samples are considered: unpinned, and Z-pinned with 0.27 % and 0.54 % areal densities. HexPly® IM7/8552 carbon/epoxy unidirectional prepreg with 0/±45 layup and 0.28 mm diameter T300/BMI pins were employed to manufacture the specimens. The Z-pinned laminates have comparable TTS with the unpinned samples in terms of the first observable load-drop. However, the TTS corresponding to the ultimate load-drop for low-density and high-density Z-pinned samples are 29 % and 38 % lower than for the unpinned ones, respectively. Z-pinned samples show less scatter than unpinned ones in terms of the ultimate TTS values. All specimens failed suddenly, i.e. with no evident damage progression. This implies that Z-pins were not able to form a progressive bridging zone to dissipate mechanical energy. Through a detailed meso-scale finite element analysis (FEA), it was found that the high through-thickness tensile residual stress in the Z-pin neighbourhood generated from the cool-down stage of cure is an important factor in causing the reduction in TTS of Z-pinned laminates. CT scan images of tested Z-pinned specimens show that the carbon-fibre pins experience fracture inside the laminates.

1. Introduction

Fibre-reinforced polymer composite laminates are weaker in the out-of-plane direction than in the plane, because fibres are absent in the through-thickness direction and plies are purely bonded by relatively low-strength polymer matrix. Thus, composite laminates are susceptible to interlaminar debond (delamination). Introducing a reinforcing phase through the thickness of composite laminates can significantly mitigate the interlaminar weakness of composite laminates. Stitching and Tufting are effective through-thickness reinforcement (TTR) methodologies, whereby continuous fibres are introduced into dry fabrics before resin infusion [1,2]. On the other hand, Z-pinning is a discrete TTR technique where small rods are inserted into prepreg laminates before curing [3].

The failure of composites can be broadly categorized into strength-based damage initiation and energy-based fracture propagation. Nearly all of the published research on Z-pinned laminates focuses on energy-based fracture [3] since mitigation of delamination propagation is deemed to be their major benefit. The influence of Z-pins on the apparent fracture toughness of laminates under mode I, mode II and mixed mode loadings have been widely studied experimentally and numerically [3–18]. To investigate the interlaminar fracture toughness enhancement performance of Z-pins, a pre-crack is normally seeded in a laminate. The laminate is loaded so that the crack propagates along a pre-defined interface and through a Z-pinned region. When the crack propagates along an interlaminar interface under a mode I dominated loading [12–16], Z-pins will first debond from the laminate, and then progressively be pulled out while exerting a frictional crack-closing force. Final failure ensues because of either complete pull-out or pin rupture. Mode II delamination resistance is also usually enhanced by Z-pins, but not to the same extent as in mode I [6–8]. A bridging zone is formed within Z-pinned regions, and the combined normal and shear tractions exerted by the TTR resist the crack growth.

A scenario in which the influence of Z-pins on initiation has been considered is in larger-scale structural tests, such as impacts [19,20], which occur in the absence of a pre-crack. Here, the critical impact force (the first sudden load drop) primarily depends on the elastic modulus [19] and mode II fracture toughness [21]. In this context, the dominance still lies with initiation fracture toughness rather than strength. Almost no work has been done using strength-based initiation tests for specimens without any pre-cracks.

The four-point bending test of a curved laminate is a strength-based initiation case. A typical example on this is an L-shaped joint used in the leading edge of aircraft wings. The L joint withstands a bending moment, and usually leads to delamination due to the high through-thickness tensile stress in the curved section [22–26]. In the open literature, only one published paper [27] experimentally studied the curved beam under four-point bending. Moreover, to the authors' knowledge, no relevant modelling work has been attempted for the aforementioned case. In Ref. [27], grooved stainless-steel Z-pins were used, and the pin surface was treated by physical and chemical means to increase the friction force between the embedded pins and the surrounding laminate. The curved beam strength was increased by 21, 27 and 42 % using 0.3 mm diameter pins and 8.7, 12 and 32 % by 0.5 mm ones, at the areal densities of 0.5, 1 and 2 %, respectively. On the contrary, Liu et al. [28] discovered that the out-of-plane tensile strength of composite laminates, as measured in the out-of-plane tensile test for cylinder shaped specimens, decreased with the introduction of T300/epoxy carbon-fibre pins with a 0.5 mm diameter. This reduction was attributed to resin-rich zone defects, resulting in a decrease of 20.2 % when the pinning density was 1.4 %.

Given the limited existing research on strength-based initiation studies for the through-thickness strength of Z-pinned laminates, as reviewed above, this study aims to investigate the impact of Z-pins on the through-thickness tensile strength (TTS) of curved composite laminates through the use of four-point bending tests. But different from Ref. [27], the most commonly used carbon-fibre composite (T300/BMI) Z-pin was used and meso-scale finite element (FE) models were built to explore factors affecting damage initiation, such as residual stresses from the cooling down process. This study provides new observations regarding the influence of Z-pins on the initiation of interlaminar cracks. The specimen design and preparation are introduced in Section 2. The four-point bending test, together with the relevant results are presented in Section 3. The numerical results are discussed and compared to the experimental ones in Section 4.

2. Specimen design and preparation

The specimens studied here are curved laminates with a layup of [0, (+45/0/-45/0)$_2$ (+45$_2$/-45$_2$/0$_2$)$_3$]$_S$ manufactured from the 180 °C cure IM7/8552 carbon/epoxy unidirectional prepreg from Hexcel and T300/BMI pins with a diameter of 0.28 mm. The geometry is shown in Fig. 1 (a). The specimen design was inspired by the work of Xu et al. [29] who used a similar specimen to embed wrinkle defects in a corner radius. That work in turn was built off the ASTM D6415/D6415 M test standard
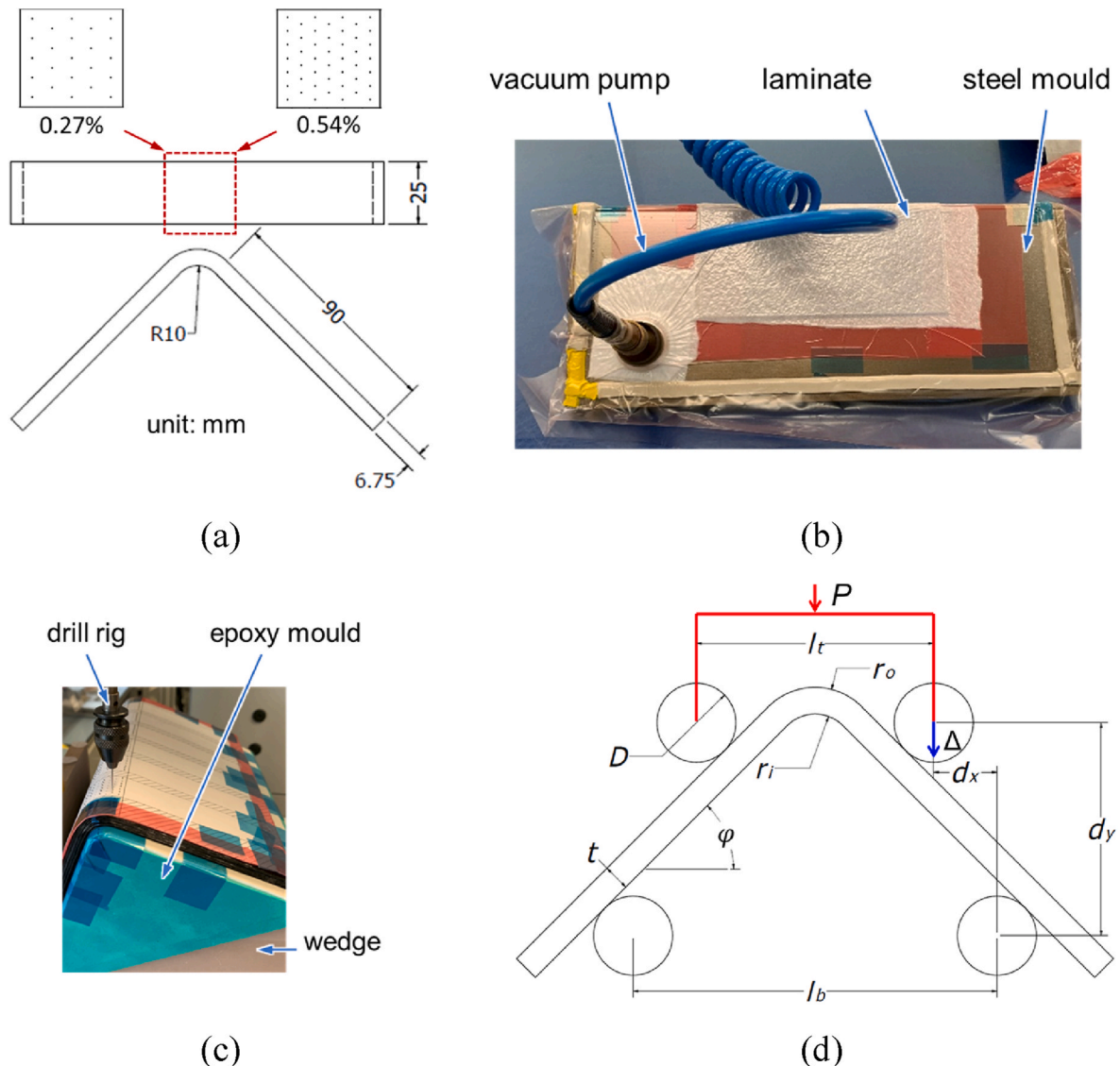

(a)

(b)

(c)

(d)

Fig. 1. (a) Sample geometry and top view of pinning layout, (b) debulking, (c) pinning, (d) variables of the test.

for laminated composites' through-thickness strength [30]. As the laminates have a curved shape, a zigzag configuration was designed for pinning to avoid the pin potential intersection at the inner surface, as shown in Fig. 1 (a). Two pinning configurations were studied. Firstly, high-density Z-pinned specimens with pin-to-pin distances of 2.1 mm and 3.5 mm in the hoop and width directions at the inner surface, respectively. This arrangement yields an aerial density of 0.54 %, calculated at the mid-plane of the curved section, with hoop and width spacing of 2.8 mm and 3.5 mm. Secondly, a lower mid-plane aerial density Z-pinned specimen of 0.27 %, with pin-to-pin distances on the inner surface of 3 mm and 5 mm in the hoop and width directions, and 4 mm and 5 mm at the mid-plane. Thus, three types of samples were manufactured in total, i.e. unpinned, 0.27 % and 0.54 % Z-pinned.

The manufacturing process consists of the following main steps:

- Align the centrelines of the prepreg and a steel mould, and layup the prepreg onto the mould. Debulking inside a sealed bag was conducted for 15 min after every four plies to reduce air content, as shown in Fig. 1 (b).
- Transfer the laminate to a high-temperature epoxy tooling board mould for pinning and insert pins into pre-drilled holes manually through the thickness of the curved section. A pair of wedges were put underneath the mould to control the pinning angle (Fig. 1 (c)).
- Cure the laminate in an autoclave, following a modified standard cure cycle [31] to account for the effects of two layers of 1.5 mm thick silicon rubbers that were applied to the top of the laminate to protect the pin ends as the laminate compacts. The rubber sheets contribute to some degree of heat isolation for the laminate; thus, it takes longer for the laminate to reach the set temperature. A preliminary test cure cycle was executed to determine a suitable extension for dwelling times. Subsequently, an additional 30 min were incorporated for each dwelling stage, to ensure a complete cure.
- Cut individual specimens from the cured laminate. Polish two side surfaces with fine sandpapers to ensure smoothness of the edges.

The mean final thickness for unpinned specimens, as well as for specimens with 0.27 % and 0.54 % Z-pinning, is 6.87 mm, 6.92 mm, and 6.95 mm, respectively. The slightly increased thickness observed in Z-pinned specimens compared to unpinned ones is attributed to the laminate swelling caused by the presence of Z-pins and the displacement of surrounding fibres [32].

3. Four-point bending test

3.1. Test set-up

The test method follows the ASTM D6415/D6415 M − 06a standard [30]. The distances between top and bottom rollers are 60 mm and 92 mm respectively (Fig. 1 (d)). The experimental set-up is shown in Fig. 2. A hydraulic-driven Instron 8872 with a 25 kN load cell was used for
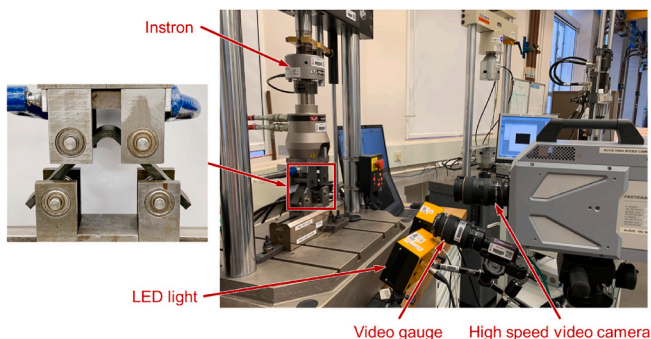

Fig. 2. Test set-up.

loading the specimens at a rate of 1 mm/min under a displacement control. A video gauge and a high-speed video camera were placed in front of the specimen to capture the failure events. The tests were stopped manually when a 50 % load drop had been observed.

3.2. Experimental results

3.2.1. Load-displacement curves

Five samples were tested in each group and individual load-displacement curves are presented in Fig. 3(a–c). In the legend, the control unpinned samples are named 'C', low-density (0.27 %) and high-density (0.54 %) Z-pinned ones are named 'L' and 'H' respectively. The load-displacement curves increase almost linearly until delamination happens. For each type of sample, the linear parts overlap, demonstrating the consistency of the test set-up. The unpinned samples tend to exhibit one large load drop corresponding to failure, albeit some smaller load reductions can be observed in the charts. However, there was no obvious damage onset corresponding to those. Four out of five 0.27 % Z-pinned samples and two out of five 0.54 % Z-pinned ones have two significant load drops. The other Z-pinned specimens exhibit only one load drop. One curve from each group was selected and plotted in Fig. 3 (d). This indicates that the curve slopes of unpinned and 0.27 % Z-pinned samples are nearly identical, while the slope of 0.54 % Z-pinned specimens is slightly smaller. The reduction in stiffness is attributed to the geometric defects, such as fibre crimping and waviness, associated with Z-pins [33].

3.2.2. Failure modes

For the unpinned samples, small edge cracks appeared near the outer surface, but they did not cause a measurable load drop, as shown in the insets P1 and P2 of Fig. 4 (a) and P1 of Fig. 4 (b). Some of these edge cracks did not propagate across the width direction and there was no load drop observed in the load-displacement curves such as the sample C3 in Fig. 4 (a). However, some of them led to delamination onset at top plies through the specimen width, and this resulted in an observable load drop, as shown in insets P2 and P3 in Fig. 4 (b) of sample C4. The generations of these stable or slowly propagating cracks near the outer surface are discussed later in Section 4. The final load drops are all due to the catastrophic delamination in the middle region, as shown in P3 of Fig. 4 (a) and P4 of Fig. 4 (b).

Regarding the Z-pinned samples, two failure modes are observed. Delamination occurred near the inner surface of some samples, resulting in a first load drop, but the specimens did not fail completely and were still able to sustain further loading until failure in the middle through-thickness region happened, such as samples L3 and H3 in Fig. 4 (c, e). The structure became more compliant after the first load drop, as a few plies near the inner surface were partially debonded from the laminate. On the other hand, some of the Z-pinned specimens did not show the near-inner-surface delamination before the catastrophic delamination in the middle through-thickness region, such as samples L1 and H4 in Fig. 4 (d, f). The first load drop of Z-pinned specimens is more pronounced compared to that of the unpinned control ones. This is because the process of initiating the first opening delamination crack is more unstable for Z-pinned specimens, as it demands more energy to fracture the rigid carbon-fibre Z-pins.

3.2.3. Through-thickness tensile strength

The Curved Beam Strength (CBS) and TTS can be calculated with the following equations according to the ASTM D6415/D6415M-06a standard [30]:

$$CBS = \left(\frac{P}{2w \cos(\varphi)} \right) \left(\frac{d_x}{\cos(\varphi)} + (D+t)\tan(\varphi) \right) \quad (1)$$

$$d_y = d_x \tan(\varphi_i) + \frac{D+t}{\cos(\varphi_i)} - \Delta \quad (2)$$
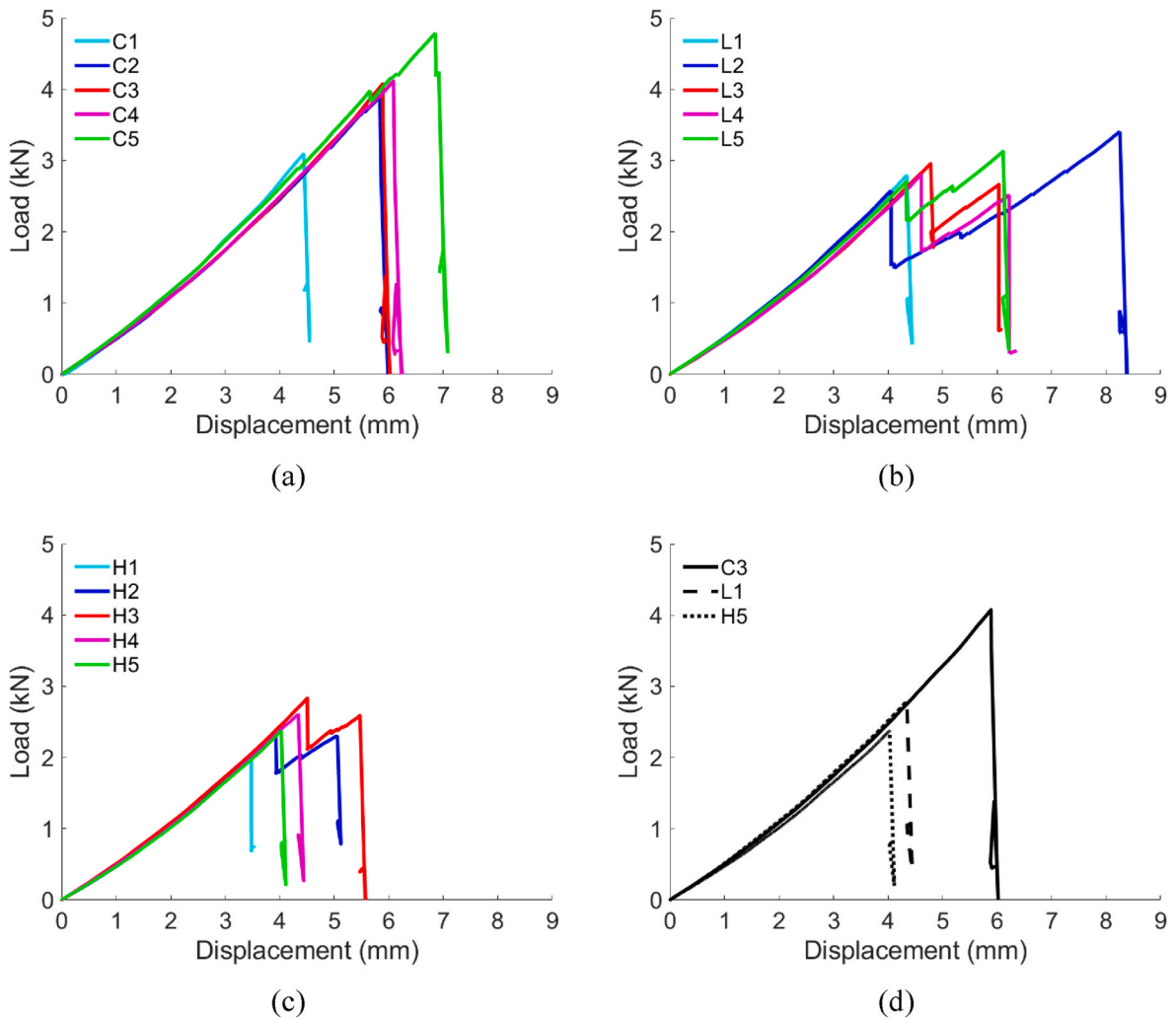
Fig. 3. Experimental load-displacement curves: (a) unpinned samples, (b) 0.27 % Z-pinned samples, (c) 0.54 % Z-pinned samples, (d) comparison of one representative curve from each sample type.

$$\varphi = sin^{-1}\left(\frac{-d_x(D+t) + d_y\sqrt{d_x^2 + d_y^2 - D^2 - 2Dt - t^2}}{d_x^2 + d_y^2}\right) \quad (3)$$

$$TTS = \frac{3 \bullet CBS}{2t\sqrt{r_i r_o}} \quad (4)$$

The variables appearing in the equations above are shown in Fig. 1 (d). P is the failure load, and Δ is the vertical relative displacement. $D = 20\,mm$ is the roller diameter. φ is the angle from horizontal to the specimen leg in degree, and $\varphi_i = 45°$ is the initial value of φ. The angle between the two specimen legs is 90°. d_x and d_y are the horizontal and vertical distances between the same-side top and bottom rollers. d_x equals to 16 mm. r_i and r_o are the inner and outer radii of the specimen, and w and t are the specimen width and thickness. The inner radius and width of the specimen are 10 mm and 25 mm respectively.

Two TTS values are calculated here, corresponding to the first observable load drop and the ultimate failure load, respectively. The experimental results are summarised in Table 1. The TTS mean values of unpinned and Z-pinned samples were compared in the chart, with standard error bars, in Fig. 5. The latter indicates that the TTS associated with the first load-drops of 0.27 % and 0.54 % Z-pinned samples is 0.5 % higher and 5.6 % lower, respectively, than that of the unpinned coupons. These small variations in initial TTS are considered statistically insignificant, as they fall within the same standard deviation range. While we

report precise numerical values for completeness, in practice, there is no notable difference between them. The ultimate load-drops of the TTS 0.27 % and 0.54 % Z-pinned samples are 29 % and 38 % lower than that of the unpinned specimens, respectively. The scatter of ultimate TTS values for the Z-pinned samples is less than for the unpinned specimens, which can be noted by the coefficient of variation in Table 1 and the standard error bars in Fig. 5.

As discussed in the introduction, Z-pins have been shown to promote resistance to crack propagation in previous research, because of the energy dissipation associated with the interlaminar crack bridging process (pull-out or failure). However, the failure of curved beams under four-point bending is in principle controlled by crack initiation, due to a relatively uniform interlaminar tensile stress in the failure region. Once delamination onset took place in the tests, the interlaminar crack quickly propagated and Z-pins were only pulled out by very short lengths before ruptured immediately, as will be discussed in detail in the next section.

The reduction of TTS in this study is mainly attributed to the through-thickness residual stresses that occur in the post-cure cool-down stage, that are strongly influenced by the introduction of the Z-pins, which is demonstrated by the finite element analysis in section 4.2. The microstructural features caused by the presence of the pins, in particular the stress concentration around the TTR holes, will additionally influence the failure. This result is in contrast to the results from Ref. [27], where the TTS increased with the introduction of metal Z-pins.
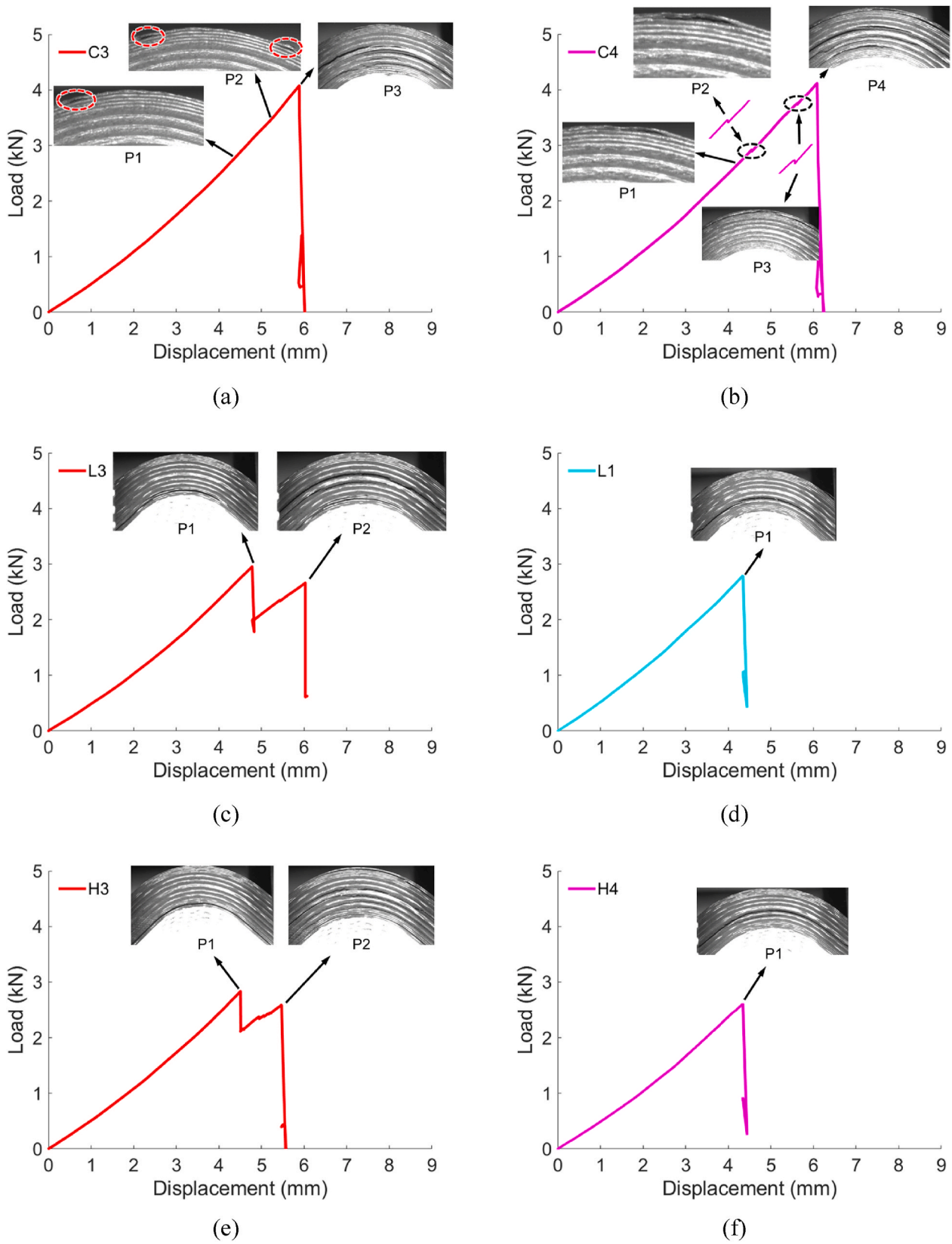
(a)

(b)

(c)

(d)

(e)

(f)

Fig. 4. Failure images: (a & b) unpinned, (c & d) 0.27 % pinned, and (e & f) 0.54 % pinned (Note: the plot colour of each sample is consistent with Fig. 3). (For interpretation of the references to colour in this figure legend, the reader is referred to the Web version of this article.)

Table 1
Experimental results of through-thickness tensile strength, (Note: '-' means this sample only has one observable load drop).

Sample ID	Unpinned		0.27 % Z-pinned		0.54 % Z-pinned	
	First TTS (MPa)	Ultimate TTS (MPa)	First TTS (MPa)	Ultimate TTS (MPa)	First TTS (MPa)	Ultimate TTS (MPa)
1	–	61.65	–	55.96	–	41.90
2	46.94	73.57	51.17	56.92	46.78	43.96
3	–	76.78	57.62	49.39	55.20	48.62
4	58.00	76.93	55.09	46.29	–	51.41
5	57.16	85.60	53.36	57.59	–	47.81
Mean	**54.03**	**74.91**	**54.31**	**53.23**	**50.99**	**46.74**
C.V.	11.4 %	11.6 %	5.0 %	9.5 %	11.7 %	8.1 %
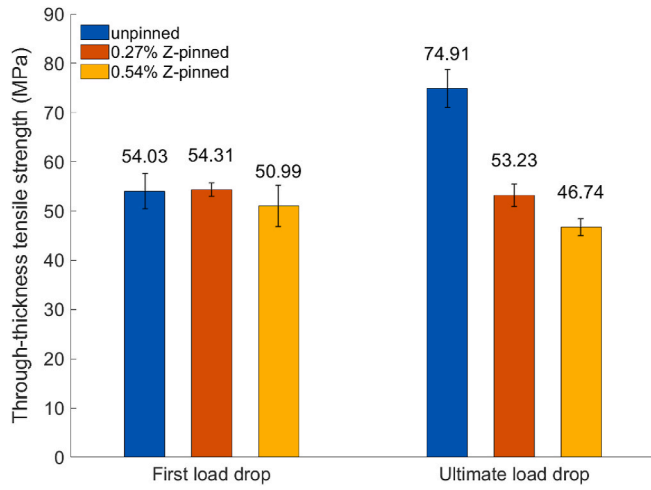
Fig. 5. Comparison of TTS between unpinned and Z-pinned samples.

The difference is likely attributable to a combination of three main factors. Firstly, the better ductility of metal pin can promote put-out and avoid pin rupture in mixed mode loading scenarios [34]. In addition, a lower curing temperature (140 °C and 125 °C) of the materials [35,36] employed in Ref. [27] results in lower residual stress. Finally, the calculated TTS of unpinned control specimens in Ref. [27] is much lower than material's transverse tensile strength. Whilst the measured TTS of a given material is not exactly the same as its transverse tensile strength, they are generally fairly similar, due to the transverse isotropy of a ply. Although the Z-pinned specimens show an improvement in TTS compared with the unpinned ones in Ref. [27], the value is still lower or just comparable to the material's transverse data property [27]. In the current study, the measured ultimate TTS of the unpinned specimen is close to the material's transverse tensile strength [31,37], indicating a reliable manufacturing quality and test set-up.

4. Result discussion

4.1. Microstructural features induced by Z-pin

Microstructural features introduced due to pinning include holes, resin pockets and fibre breakage and waviness around the resin pockets [3]. In the curved specimens considered here, the pinning areal density increases from the outer surface to the inner one. Thus, the microstructural disruption of the laminates architecture due to pinning is more severe near the inner surface. This might be the reason why near-inner-surface delamination was observed in some pinned specimens. Furthermore, these microstructural features are also affected by TTR misalignment, which is an unavoidable feature of Z-pinning [38]. The misalignment angle differs from pin to pin and from specimen to

specimen. Potentially, pin misalignment could reduce the distance between adjacent pins near the inner surface, thus intensifying stress concentration near the pinned holes [39]. It may also cause some of the pinned specimens to experience a near-inner-surface crack.

4.2. Residual stress analysis

A high-fidelity FE model was built and run in Abaqus®/Explicit to study the effect of Z-pinning on the residual stress field generated from the post-cure cool-down process. The model was created with an in-house versatile mesh generation code, which was written by combining Python and MATLAB®. The generated FE model of a low-density Z-pinned sample is shown in Fig. 6.

The eye-shape resin-rich zones are modelled as shown in Fig. 6 (d). Because of the distinct orientation of resin pockets in each angled ply, the resin-rich zones are individually partitioned for each ply of the laminate then meshed, based on the geometric description in Ref. [4]. Cohesive elements were inserted between different-angled plies of the laminate to simulate delamination. Node-to-surface tie constraints were defined between interlaminar cohesive layers and their adjacent plies. The pin/laminate interface was modelled with cohesive elements' behaviour plus a Coulomb friction law through the general contact. 8-Node three-dimensional COH3D8 elements were adopted for the cohesive elements, while the resin pockets and laminate were built using single-integration-point solid elements (C3D8R). For the cohesive elements [40], the quadratic nominal stress criterion (with an exponent of 1) in Eq. (5) was used for the damage initiation, while the damage propagation obeys the energy-based power law in Eq. (6). The damage variable D is defined in Eq. (7).

$$\left\{\frac{\langle t_n \rangle}{\sigma_I^{\max}}\right\}^2 + \left\{\frac{t_s}{\sigma_{II}^{\max}}\right\}^2 + \left\{\frac{t_t}{\sigma_{III}^{\max}}\right\}^2 = 1 \tag{5}$$

$$\left\{\frac{G_n}{G_{IC}}\right\}^a + \left\{\frac{G_s}{G_{IIC}}\right\}^a + \left\{\frac{G_t}{G_{IIIC}}\right\}^a = 1 \tag{6}$$

$$D = \frac{\delta_m^f \left(\delta_m^{max} - \delta_m^o\right)}{\delta_m^{max} \left(\delta_m^f - \delta_m^o\right)} \tag{7}$$

In the equations, $\sigma_I^{\max}$, $\sigma_{II}^{\max}$ and $\sigma_{III}^{\max}$ represent the maximum stress under mode I, II & III loadings, respectively. t_n, t_s and t_t are the normal and two shear traction stresses. G_{IC}, G_{IIC} and G_{IIIC} represent the critical fracture energies under three modes. G_n, G_s and G_t are the work done by the traction in three nominal directions. δ_m^o and δ_m^f denote the relative displacement at the damage initiation and interface failure. δ_m^{max} is the maximum relative displacement during loading.

A temperature field with a magnitude of −160 °C, representing the difference from the cure stage of 180 °C to the room temperature of 20 °C, is applied to all nodes of the specimen to simulate the post-cure cool-down process. The rollers were assembled in place with surface-to-surface contact to the laminate in the cure step to ensure the inheritance of the final stress state after the cure step as the initial stress state for the mechanical loading step. A fixed mass scaling was applied to the whole model with a target time increment of 10^{-6} from the beginning of the step to speed up the simulation without invoking excessive kinetic energy. Following a convergence study, a size of 0.25 mm was found to be sufficient for both the cohesive elements (COH3D8) and ply elements (C3D8R) of the curved section. Hence, the in-plane mesh sizes for both ply and cohesive elements in the curved region were controlled to be equal to or less than 0.25 mm for both unpinned and Z-pinned models.

The input material properties of the laminate and pin are taken from literature [4,41], and the cohesive element properties refer to Refs. [4, 31,41–44]. The input values are summarised in Table 2, in which E is the Young's modulus, G is the shear modulus, ν is the Poisson's ratio, α is the thermal expansion coefficient, K is the stiffness of cohesive elements and
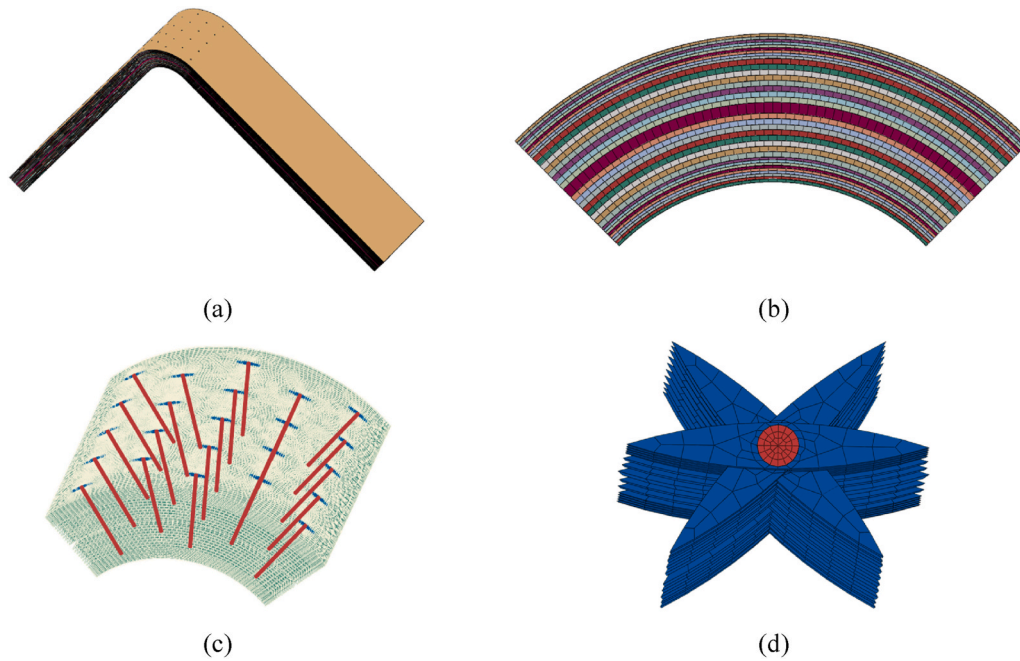
Fig. 6. FE model of the 0.27 % Z-pinned sample: (a) specimen model, (b) section view of the curved region, (c) the curved region with pins highlighted, (d) a pin and surrounding resin pockets.

Table 2
Input material properties for the post-cure cool-down simulation [4,31,41–44].

Properties of IM7/8552 ply										
E_{11} (GPa)	E_{22} (GPa)	E_{33} (GPa)	G_{12} (GPa)	G_{13} (GPa)	G_{23} (GPa)	ν_{12}	ν_{13}	ν_{23}	α_{11} (°C^{-1})	α_{22}, α_{33} (°C^{-1})
161	11.4	11.4	5.17	5.17	3.98	0.32	0.32	0.436	0	3e^{-5}

Properties of T300/BMI Z-pin										
E_{11} (GPa)	E_{22} (GPa)	E_{33} (GPa)	G_{12} (GPa)	G_{13} (GPa)	G_{23} (GPa)	ν_{12}	ν_{13}	ν_{23}	α_{11} (°C^{-1})	α_{22}, α_{33} (°C^{-1})
144	7.31	7.31	4.45	4.45	2.63	0.25	0.25	0.39	0	3e^{-5}

8552 Resin			
E (GPa)	G (GPa)	ν	α (°C^{-1})
4.56	1.67	0.37	6.5e^{-5}

Properties of interlaminar cohesive elements								
G_{IC} (N/mm)	G_{IIC} (N/mm)	G_{IIIC} (N/mm)	σ_I^{max} (MPa)	σ_{II}^{max} (MPa)	σ_{III}^{max} (MPa)	K_I (GPa)	K_{II} (GPa)	K_{III} (GPa)
0.2	1.0	1.0	90	110	110	100	100	100

Properties of pin/laminate interface									
G_{IC} (N/mm)	G_{IIC} (N/mm)	G_{IIIC} (N/mm)	σ_I^{max} (MPa)	σ_{II}^{max} (MPa)	σ_{III}^{max} (MPa)	K_I (GPa)	K_{II} (GPa)	K_{III} (GPa)	μ
0.01	1.0	1.0	60	90	90	100	100	100	0.8

μ is the Coulomb friction coefficient. The subscripts '1', '2' and '3' represent the fibre direction, transverse direction, and through-thickness direction, respectively. It is worth noting that the low value of G_{IC} for the pin/laminate interface is attributed to the weakening of the interface during the post-cooling-down process, particularly evident in local mode I loading of the pin/laminate interface, as validated in Ref. [4].

The modelling result shows that through-thickness tensile stress in the middle section of an unpinned laminate after cool-down is very low (up to 3.6 MPa) as shown in Fig. 7 (a). After adding pins, the pins tend to oppose the through-thickness contraction of the laminate due to the mismatch between the through-thickness thermal expansion coefficients of the carbon-fibre pin and the laminate. Thus, in Fig. 7 (b, c), the through-thickness tensile stress in the resin pockets reaches 100 MPa, and consequently the pin is under compression with a stress peak of

about −384 MPa. The residual tensile stress in the Z-pinned laminates locally researches 33 MPa in proximity of the resin pockets (see Fig. 7 (b, c) with pins and resin pockets removed). In summary, the presence of Z-pins introduces high residual stress within the laminate and especially around the pins, due to the post-cure cool-down. The delamination observed in Z-pinned laminates is thus expected to initiate close to the pins.

4.3. Failure of Z-pins

The Bridging behaviour of T300/BMI Z-pins is briefly reviewed below, before describing the Z-pin failure mode observed in the tested specimens. When studying the Z-pin bridging mechanisms, the most used test set-up entails inserting a single pin into two square laminate blocks, separated by a thin layer of release film at the middle plane. The
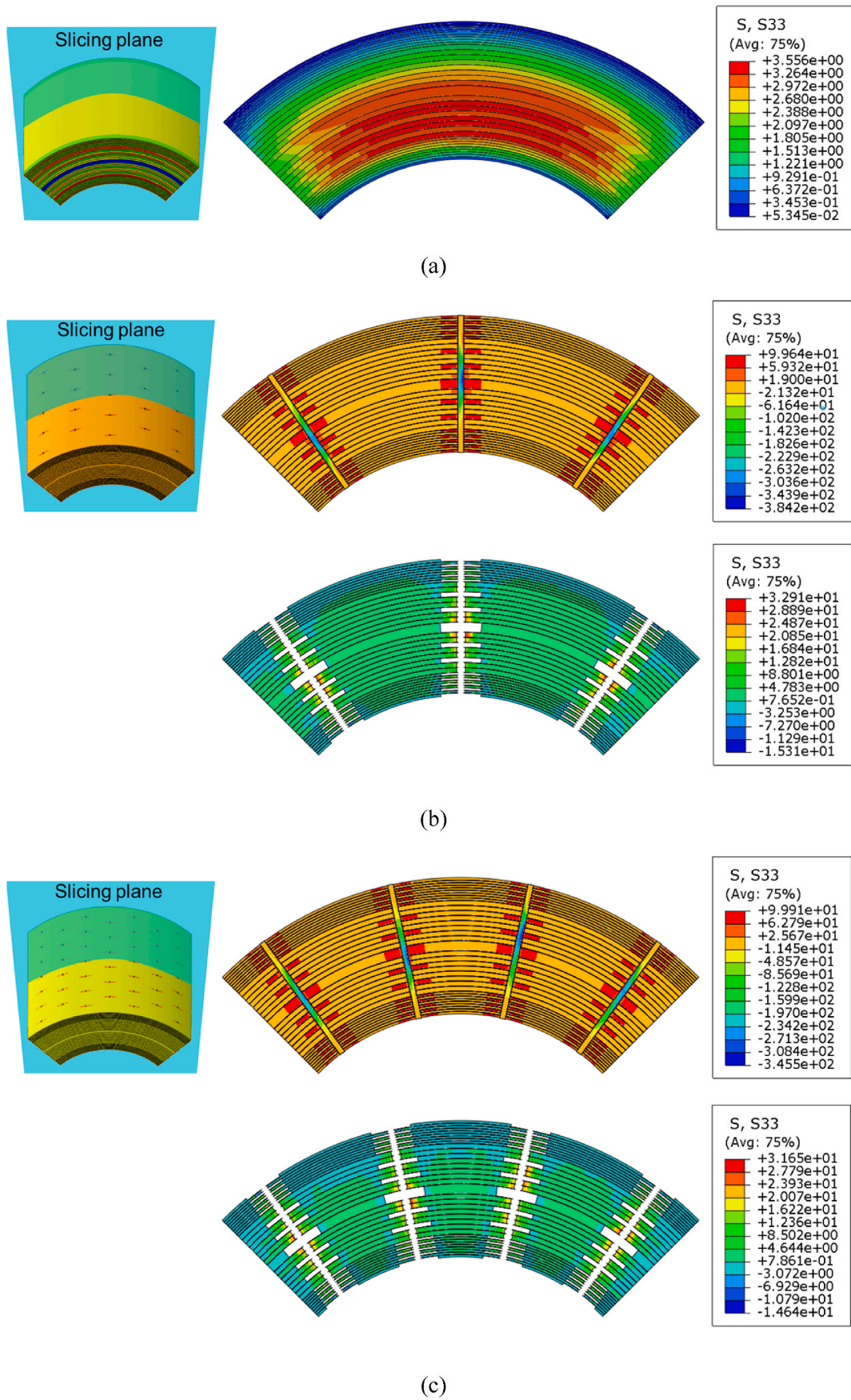
Fig. 7. Modelling results of through-thickness normal stress after cool-down: (a) unpinned, (b) 0.27 % Z-pinned, (c) 0.54 % Z-pinned, (Resin pockets and pins are shown and removed in (b) and (c), respectively.).

blocks are then separated under imposed opening and sliding displacements to simulate bridging under mode I, mixed mode and mode II. Typical load-displacement curves of single T300/BMI carbon fibre composites pin under pull-out (mode I) and shear (mode II) loading are presented in Fig. 8 (a, b). For mode I dominated loading, the pin debonds from the laminate at very small applied displacements, and then it is gradually pulled out. The corresponding pull-out force decreases with the applied displacement. Note a sharp peak load may not be observed under mode I conditions if the pin/laminate bond is significantly weakened during the post-cure cool-down. In mode II dominated loading, the pin deforms under shear and bending, until it eventually fails catastrophically. The corresponding bridging force is monotonically increasing with the applied sliding displacement. The failure mode of T300/BMI Z-pins under mixed mode loading is a combination of the mode I frictional pull-out and mode II shear rupture, with a transition between the two regimes that occurs within a characteristic mode-mixity range [38], as illustrated in Fig. 8 (c).

In order to reveal the actual failure mode of pins inside the tested coupons, the Z-pinned specimens were examined using a modified 225 kVp Nikon/Xtek HMX CT scanner. The pin and laminate materials are quite similar in terms of composition, thus the contrast from different linear attenuation coefficients of the constituents is small [45]. Hence, the tested coupons were soaked in a bath of zinc iodide penetrant for 2 days before the scan to more clearly reveal the presence of cracks [46]. The legs of samples were trimmed off to reduce the scanning volume. One 0.27 % pinned (L3) and one 0.54 % pinned (H4) sample were examined via X-ray CT.

CT scan images show that 3 out of 23 pins of the 0.27 % pinned sample were intact or only partially broken, and the remaining ones had failed as shown in Fig. 9 (a). All the 46 pins of the 0.54 % Z-pinned sample were found to have failed (Fig. 9 (b)). The middle column pins in Fig. 9 are in principle subject to pure mode I. Their fracture can most likely be attributed to a combination of factors: 1) the relatively thick laminate, leading to potential tensile failure of the pin due to high interfacial stress and an extended bonding area [47]; and 2) pin misalignment, causing transverse shear stress on the pins. The side-column pins are under mixed mode loading. Those pins were fractured under an obvious shear deformation, such as that shown in

insets (1) and (3) in Fig. 9 (b), due to the sliding of adjacent plies.

4.4. Free edge stress analysis

As mentioned in the previous section, local cracks were observed near the top surface of unpinned specimens, at the 0/45 and 0/-45 interfaces as shown in Fig. 10 (a). In order to examine if it is due to the high stress level developed at free edges [29,48], a stress analysis was carried out with an unpinned model in Abaqus®/Explicit. The modelling set-up and definition are the same with the Z-pinned model mentioned above. The elements of an edge strip in the centre of the curved section (Fig. 10 (b)) were selected for the quantitative analysis. The failure of the laminate is influenced by a coupling effect of delamination and in-plane shear s_{12}. Currently, there is no quantitative equation explicitly combining these two effects. Hence, they are treated as two mathematically uncoupled phenomena here, recognising that both contribute to the laminate failure. For the delamination, a damage index di was defined with a quadratic law [48–50] by using the through-thickness tensile stress s_{33}, and shear stresses s_{13}, s_{23}, as given in Eq. (8).

$$di = \left(\frac{s_{33}}{\sigma_I^{max}}\right)^2 + \left(\frac{\sqrt{s_{13}^2 + s_{23}^2}}{\sigma_{II}^{max}}\right)^2 \tag{8}$$

There are two elements in the through-thickness direction for each ply. A mesh convergence study was carried out, with the element sizes in the length and width directions assigned as 0.05×0.01, 0.1×0.02, and 0.2×0.04 (unit: mm) respectively. The result was found to converge, and the three models provide the same trend of stress distribution for the near-edge elements with very little difference. Simulation results of the 0.05×0.01 model are plotted in Fig. 10 (c, d). Fig. 10 (c) shows that the delamination damage index of the top plies is higher than the bottom plies, but much lower compared with the mid through-thickness region. The maximum di is attained at the middle plies, which agrees with the catastrophic delamination location observed in experiments (Fig. 4 (a, b)). Fig. 10(d) gives the distribution of in-plane shear stress s_{12}. The latter increases from the middle to the inner and outer surfaces and is high at the top 45° and −45° plies. The in-plane shear failure most likely promotes the delamination within the top plies, while the lower di of the
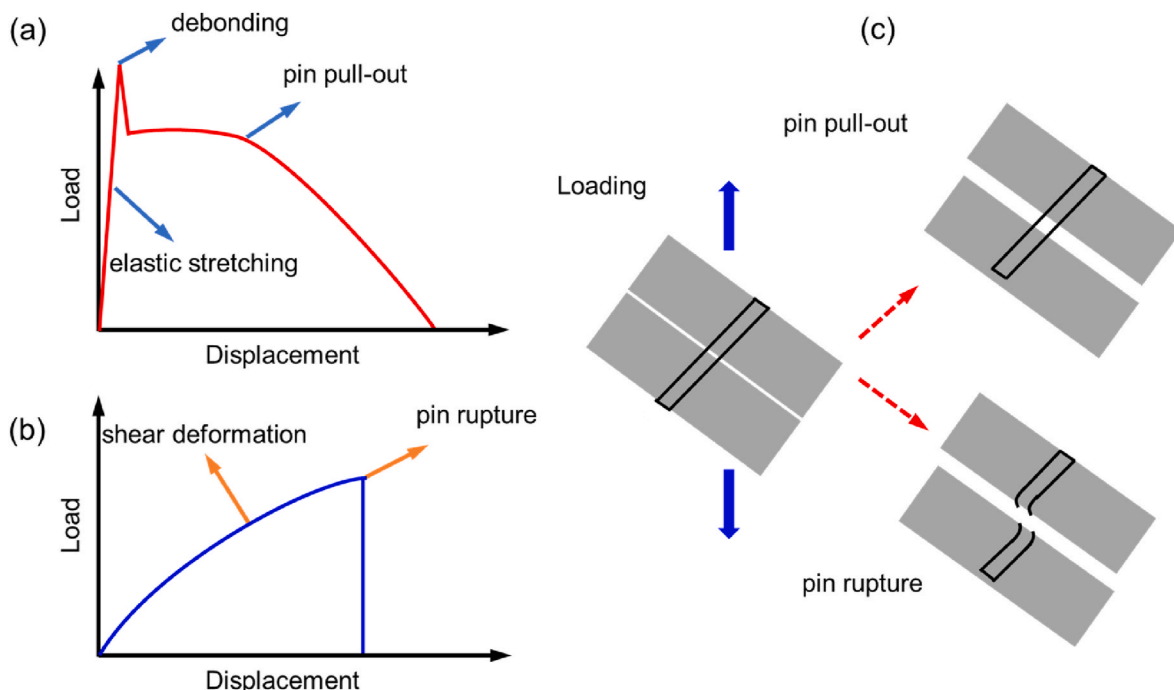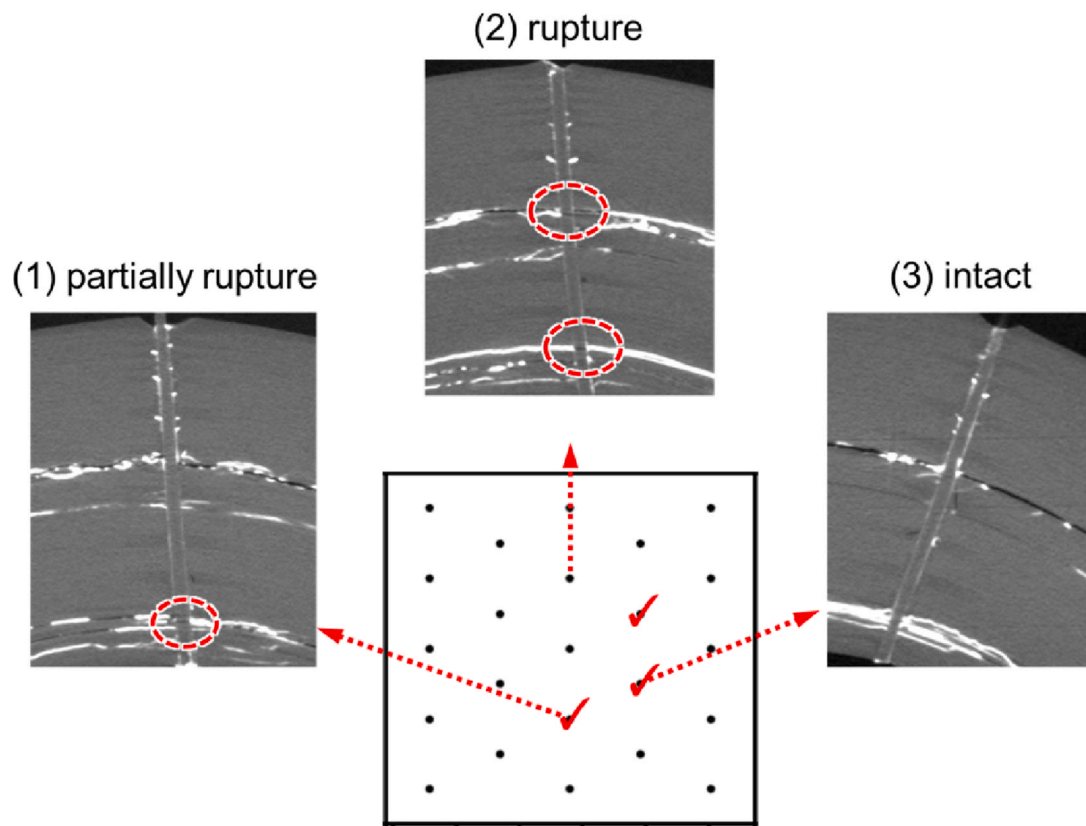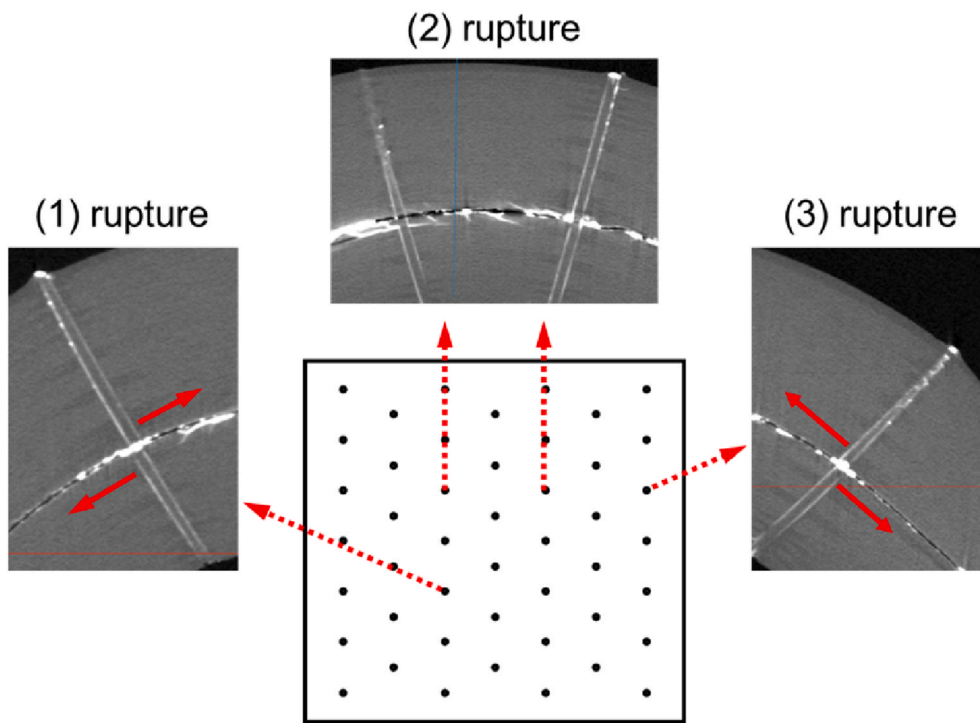

Fig. 8. Schematic illustration of Z-pin bridging and failure modes: (a) mode I bridging curve, (b) mode II bridging curve, (c) pin failures under mixed mode.
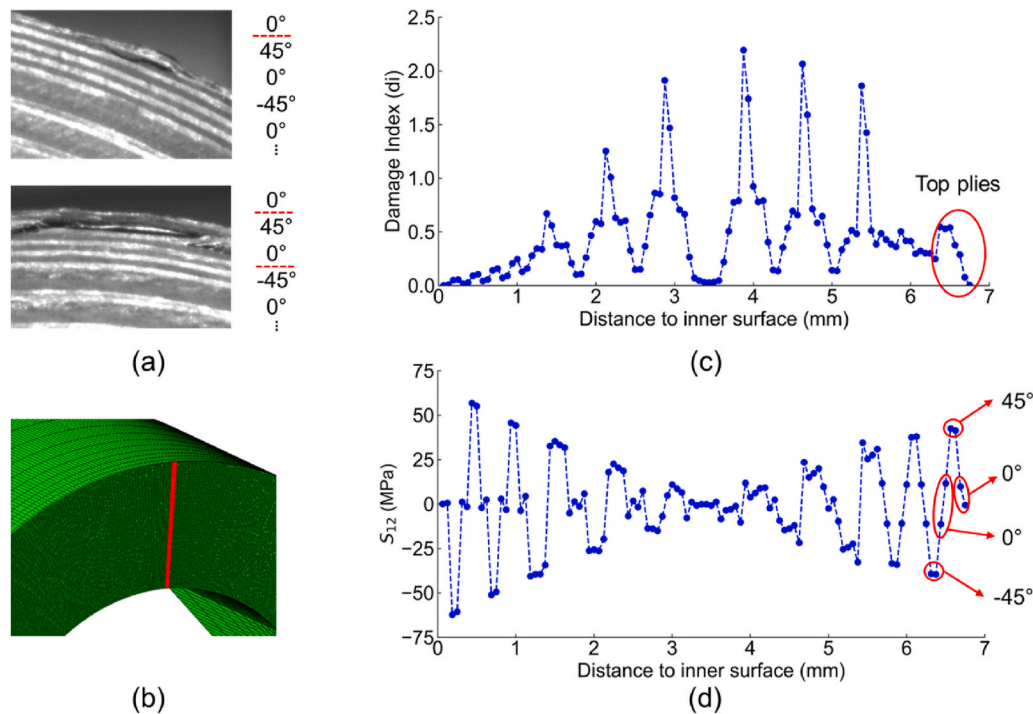
Fig. 9. CT scan images of tested Z-pinned specimens and top view of specimen pinned region: (a) 0.27 % Z-pinned, (b) 0.54 % Z-pinned (Note: '✓' is the symbol of partially broken or intact pins).

Fig. 10. (a) Cracks observed in the test, (b) FE model with selected edge-elements highlighted, (c) plot of delamination damage index, (d) plot of in-plane shear stress.

inner plies indicates no delamination, even though the in-plane shear stress is high. Apart from that, manufacturing defects such as wrinkles and voids may as well promote edge cracks.

5. Conclusions

In addition to the well-explored crack propagation resisting ability of Z-pinning in flat panels, the effects of traditional carbon-fibre Z-pins on the through-thickness tensile strength of curved laminates was here studied. This focusses on the influence of the Z-pins on crack initiation, rather than the more conventional crack propagation case when compared to studies on Z-pinned laminates reported in the open literature.

It was found that the ultimate TTS of 0.27 % and 0.54 % Z-pinned samples are 29 % and 38 % lower than unpinned ones with less experimental scatter. The pins were mostly ruptured during the test without forming a large bridging zone to dissipate the mechanical energy, since the loaded region of the specimens has a relatively uniform stress state, causing them to fail suddenly. The meso-scale FE modelling result shows that the residual interlaminar stress generated from the post-cure cool-down stage is tensile in nature and very high in the pin proximity. The pins also cause in-plane defects in the laminate, such as resin pockets and fibre waviness, which combined with high residual stresses, promote the initiation of cracks. It is thus demonstrated, that whilst Z-pinning can have a positive effect for application cases where large propagating cracks need to be controlled, care should be taken in their use for cases where failure is initiation dominated. In these cases, the use of Z-pins could be detrimental.

The FE models in this study are designed to understand the initiation of damage. Analysing the progressive damage process and predicting ultimate failure demands a further level of complexity that will be a significant focus of future work. Additionally, exploring the influence of various geometric configurations, such as increasing the laminate thickness for a larger thickness-to-radius ratio, will be beneficial.

CRediT authorship contribution statement

Mudan Chen: Writing – original draft, Validation, Software, Methodology, Investigation, Formal analysis. **Bing Zhang:** Writing – review & editing, Supervision, Software, Methodology, Formal analysis. **Giuliano Allegri:** Writing – review & editing, Supervision, Methodology. **Stephen R. Hallett:** Writing – review & editing, Supervision, Project administration, Methodology, Conceptualization.

Declaration of competing interest

The authors declare that they have no known competing financial interests or personal relationships that could have appeared to influence the work reported in this paper.

Data availability

Data will be made available on request.

Acknowledgements

References

[1] Dransfield K, Baillie C, Mai Y-W. Improving the delamination resistance of CFRP by stitching—a review. Compos Sci Technol 1994;50:305–17. https://doi.org/10.1016/0266-3538(94)90019-1.

[2] Dell'Anno G, Treiber JWG, Partridge IK. Manufacturing of composite parts reinforced through-thickness by tufting. Robot Comput Integrated Manuf 2016;37: 262–72. https://doi.org/10.1016/j.rcim.2015.04.004.

[3] Mouritz AP. Review of z-pinned laminates and sandwich composites. Compos Appl Sci Manuf 2020;139:106128. https://doi.org/10.1016/j.compositesa.2020.106128.

[4] Zhang B, Allegri G, Yasaee M, Hallett SR. Micro-mechanical finite element analysis of Z-pins under mixed-mode loading. Compos Appl Sci Manuf 2015;78:424–35. https://doi.org/10.1016/j.compositesa.2015.07.006.

[5] Cui H, Yasaee M, Hallett SR, Partridge IK, Allegri G, Petrinic N. Dynamic bridging mechanisms of through-thickness reinforced composite laminates in mixed mode delamination. Compos Appl Sci Manuf 2018;106:24–33. https://doi.org/10.1016/j.compositesa.2017.11.017.

[6] Cui H, Yasaee M, Kalwak G, Pellegrino A, Partridge IK, Hallett SR, et al. Bridging mechanisms of through-thickness reinforcement in dynamic mode I&II delamination. Compos Appl Sci Manuf 2017;99:198–207. https://doi.org/10.1016/j.compositesa.2017.04.009.

[7] M'membe B, Gannon S, Yasaee M, Hallett SR, Partridge IK. Mode II delamination resistance of composites reinforced with inclined Z-pins. Mater Des 2016;94: 565–72. https://doi.org/10.1016/j.matdes.2016.01.051.

[8] Yasaee M, Mohamed G, Hallett SR. Interaction of Z-pins with multiple mode II delaminations in composite laminates. Exp Mech 2016;56:1363–72. https://doi.org/10.1007/s11340-016-0175-9.

[9] Yasaee M, Mohamed G, Pellegrino A, Petrinic N, Hallett SR. Strain rate dependence of mode II delamination resistance in through thickness reinforced laminated composites. Int J Impact Eng 2017;107:1–11. https://doi.org/10.1016/j.ijimpeng.2017.05.003.

[10] Melro AR, Serra J, Allegri G, Hallett SR. An energy-equivalent bridging map formulation for modelling delamination in through-thickness reinforced composite laminates. Int J Solid Struct 2020;202:153–65. https://doi.org/10.1016/j.ijsolstr.2020.06.018.

[11] Mohamed G, Allegri G, Yasaee M, Hallett SR. Cohesive element formulation for z-pin delamination bridging in fibre reinforced laminates. Int J Solid Struct 2018; 132–133:232–44. https://doi.org/10.1016/j.ijsolstr.2017.05.037.

[12] Pegorin F, Pingkarawat K, Daynes S, Mouritz AP. Influence of z-pin length on the delamination fracture toughness and fatigue resistance of pinned composites. Compos B Eng 2015;78:298–307. https://doi.org/10.1016/j.compositesb.2015.03.093.

[13] Pingkarawat K, Mouritz AP. Comparative study of metal and composite z-pins for delamination fracture and fatigue strengthening of composites. Eng Fract Mech 2016;154:180–90. https://doi.org/10.1016/j.engfracmech.2016.01.003.

[14] Hoffmann J, Sabban J, Scharr G. Pullout performance of circumferentially notched z-pins in carbon fiber reinforced laminates. Compos Appl Sci Manuf 2018;110: 197–202. https://doi.org/10.1016/j.compositesa.2018.05.002.

[15] Mouritz AP, Koh TM. Re-evaluation of mode I bridging traction modelling for z-pinned laminates based on experimental analysis. Compos B Eng 2014;56: 797–807. https://doi.org/10.1016/j.compositesb.2013.09.016.

[16] Santana de Vega E, Allegri G, Zhang B, Hamerton I, Hallett SR. Improving the delamination bridging performance of Z-pins through the use of a ductile matrix. Compos Appl Sci Manuf 2022;163:107241. https://doi.org/10.1016/j.compositesa.2022.107241.

[17] Liu W, Jin K, Cheng J, Yan B, Yin M, Sang C. Experimental and numerical investigations on the mode I delamination growth behavior of reinforced laminates via a ZPI (Z-pin pre-hole insertion) technique. J Compos Mater 2023;57:3295–315. https://doi.org/10.1177/00219983231184298.

[18] Teng X, Xu Y, Zhang W, Hui X, Liu W, Ma C. Improving Mode II delamination resistance of curved CFRP laminates by a Pre-Hole Z-pinning (PHZ) process. Chin J Aeronaut 2022;36. https://doi.org/10.1016/j.cja.2022.09.018.

[19] Zhang X, Hounslow L, Grassi M. Improvement of low-velocity impact and compression-after-impact performance by z-fibre pinning. Compos Sci Technol 2006;66:2785–94. https://doi.org/10.1016/j.compscitech.2006.02.029.

[20] Cochrane AD, Serra J, Lander JK, Böhm H, Wollmann T, Hornig A, et al. Experimental investigation of high strain-rate, large-scale crack bridging behaviour of z-pin reinforced tapered laminates. Compos Appl Sci Manuf 2022;155:106825. https://doi.org/10.1016/j.compositesa.2022.106825.

[21] Suemasu H, Ichiki M, Aoki Y. Analytical approach for evaluation of impact damage in nonlinear quasi-isotropic plates of arbitrary boundary conditions. Adv Compos Mater 2023;32:324–49. https://doi.org/10.1080/09243046.2022.2087581.

[22] Charrier J-S, Laurin F, Carrere N, Mahdi S. Determination of the out-of-plane tensile strength using four-point bending tests on laminated L-angle specimens with different stacking sequences and total thicknesses. Compos Appl Sci Manuf 2016;81:243–53. https://doi.org/10.1016/j.compositesa.2015.11.018.

[23] González-Cantero JM, Graciani E, López-Romano B, París F. Competing mechanisms in the unfolding failure in composite laminates. Compos Sci Technol 2018;156:223–30. https://doi.org/10.1016/j.compscitech.2017.12.022.

[24] Ranz D, Cuartero J, Miravete A, Miralbes R. Experimental research into interlaminar tensile strength of carbon/epoxy laminated curved beams. Compos Struct 2017;164:189–97. https://doi.org/10.1016/j.compstruct.2016.12.010.

[25] Andraju LB, Raju G. Continuum and cohesive zone damage models to study intra/inter-laminar failure of curved composite laminates under four-point bending.

[26] Zou X, Yan S, Matveev M, Rouse JP, Jones IA. Experimental and numerical investigation of interface damage in composite L-angle sections under four-point bending. J Compos Mater 2020:0021998320943659. https://doi.org/10.1177/0021998320943659.

[27] Ju H, Nguyen K-H, Chae S-S, Kweon J-H. Delamination strength of composite curved beams reinforced by grooved stainless-steel Z-pins. Compos Struct 2017; 180:497–506. https://doi.org/10.1016/j.compstruct.2017.08.018.

[28] Liu Y, Cai L, Ding H, Xu Q. Out-of-plane properties and failure mechanism of composite laminates reinforced with carbon Z-pins. Appl Compos Mater 2023;30: 379–97. https://doi.org/10.1007/s10443-022-10087-4.

[29] Xu X, Jones MI, Ali H, Wisnom MR, Hallett SR. Effect of out-of-plane wrinkles in curved multi-directional carbon/epoxy laminates. Compos Sci Technol 2020;197: 108282. https://doi.org/10.1016/j.compscitech.2020.108282.

[30] D30 Committee. Test method for measuring the curved beam strength of a fiber-reinforced polymer-matrix composite. ASTM International; 2013. https://doi.org/10.1520/D6415_D6415M-06AR13.

[31] Prepreg data sheet | Hexcel. 2020. https://www.hexcel.com.

[32] Chang P, Mouritz AP, Cox BN. Properties and failure mechanisms of z-pinned laminates in monotonic and cyclic tension. Compos Appl Sci Manuf 2006;37: 1501–13. https://doi.org/10.1016/j.compositesa.2005.11.013.

[33] Mouritz AP, Cox BN. A mechanistic interpretation of the comparative in-plane mechanical properties of 3D woven, stitched and pinned composites. Compos Appl Sci Manuf 2010;41:709–28. https://doi.org/10.1016/j.compositesa.2010.02.001.

[34] M'membe B, Yasaee M, Hallett SR, Partridge IK. Effective use of metallic Z-pins for composites' through-thickness reinforcement. Compos Sci Technol 2019;175: 77–84. https://doi.org/10.1016/j.compscitech.2019.02.024.

[35] Shin Y-C, Kim S-M. Enhancement of the interlaminar fracture toughness of a carbon-fiber-reinforced polymer using interleaved carbon nanotube buckypaper. Appl Sci 2021;11:6821. https://doi.org/10.3390/app11156821.

[36] Hong H, Bae KJ, Jung H, Oh Y, You N-H, Lee J-C, et al. Preparation and characterization of carbon fiber reinforced plastics (CFRPs) incorporating through-plane-stitched carbon fibers. Compos Struct 2022;284:115198. https://doi.org/10.1016/j.compstruct.2022.115198.

[37] Seon G, Makeev A, Schaefer JD, Justusson B. Measurement of interlaminar tensile strength and elastic properties of composites using open-hole compression testing and digital image correlation. Appl Sci 2019;9:2647. https://doi.org/10.3390/app9132647.

[38] Yasaee M, Lander JK, Allegri G, Hallett SR. Experimental characterisation of mixed mode traction–displacement relationships for a single carbon composite Z-pin. Compos Sci Technol 2014;94:123–31. https://doi.org/10.1016/j.compscitech.2014.02.001.

[39] Toubal L, Karama M, Lorrain B. Stress concentration in a circular hole in composite plate. Compos Struct 2005;68:31–6. https://doi.org/10.1016/j.compstruct.2004.02.016.

[40] Abaqus analysis user's guide. 6.14; 2023. http://130.149.89.49:2080/v6.14/books/usb/default.htm.

[41] Hallett SR, Green BG, Jiang WG, Wisnom MR. An experimental and numerical investigation into the damage mechanisms in notched composites. Compos Appl Sci Manuf 2009;40:613–24. https://doi.org/10.1016/j.compositesa.2009.02.021.

[42] Lemanski SL, Wang J, Sutcliffe MPF, Potter KD, Wisnom MR. Modelling failure of composite specimens with defects under compression loading. Compos Appl Sci Manuf 2013;48:26–36. https://doi.org/10.1016/j.compositesa.2012.12.007.

[43] Nikishkov Y, Makeev A, Seon G. Progressive fatigue damage simulation method for composites. Int J Fatig 2013;48:266–79. https://doi.org/10.1016/j.ijfatigue.2012.11.005.

[44] Lee J, Soutis C. Measuring the notched compressive strength of composite laminates: specimen size effects. Compos Sci Technol 2008;68:2359–66. https://doi.org/10.1016/j.compscitech.2007.09.003.

[45] Garcea SC, Wang Y, Withers PJ. X-ray computed tomography of polymer composites. Compos Sci Technol 2018;156:305–19. https://doi.org/10.1016/j.compscitech.2017.10.023.

[46] Xu X, Sun X, Wisnom MR. Initial R-curves for trans-laminar fracture of quasi-isotropic carbon/epoxy laminates from specimens with increasing size. Compos Sci Technol 2021;216:109077. https://doi.org/10.1016/j.compscitech.2021.109077.

[47] Mouritz AP, Koh TM. Re-evaluation of mode I bridging traction modelling for z-pinned laminates based on experimental analysis. Compos B Eng 2014;56: 797–807. https://doi.org/10.1016/j.compositesb.2013.09.016.

[48] Fletcher TA, Kim T, Dodwell TJ, Butler R, Scheichl R, Newley R. Resin treatment of free edges to aid certification of through thickness laminate strength. Compos Struct 2016;146:26–33. https://doi.org/10.1016/j.compstruct.2016.02.074.

[49] Jiang W-G, Hallett SR, Green BG, Wisnom MR. A concise interface constitutive law for analysis of delamination and splitting in composite materials and its application to scaled notched tensile specimens. Int J Numer Methods Eng 2007;69:1982–95. https://doi.org/10.1002/nme.1842.

[50] Selvaraj J, Kawashita LF, Hallett SR. Mesh independent modelling of tensile failure in laminates using mixed-time integration in explicit analysis. Eng Fract Mech 2022;259:108113. https://doi.org/10.1016/j.engfracmech.2021.108113.